Direct electric current control of hyperchaotic packets of dissipative dark envelope solitons in a magnonic crystal active ring resonator

Anastasia S. Bir,[1] Sergei V. Grishin,[1,*] Andrei A. Grachev,[1] Olga I. Moskalenko,[1] Alexey N. Pavlov,[1] Dmitrii V. Romanenko,[1] Valentin N. Skorokhodov,[1] and Sergei A. Nikitov[1,2]

[1] *Kotelnikov Institute of Radioengineering and Electronics of RAS, Moscow 125009, Russia*

[2] *Saratov State University, Saratov 410012, Russia*

(Received 3 August 2023; revised 27 January 2024; accepted 19 March 2024; published 3 April 2024; corrected 24 April 2024)

The research experimentally demonstrates the direct electric current control of hyperchaotic packets of dissipative dark envelope solitons that are self-generated in a microwave active ring resonator containing two nonlinear elements: a one-dimensional magnonic crystal (MC) with dynamic line defect and a transistor amplifier. The hyperchaotic packets of dissipative dark envelope solitons are formed at a magnetostatic surface spin wave (MSSW) propagating in the MC and taking part both in three-wave nonlinear spin-wave processes of decay and confluence. The transistor amplifier operates in output-power saturation mode. The direct electric current flowing through a copper wire placed along the longitudinal axis of the MC creates the dynamic line defect that effectively controls a duty factor of dissipative dark envelope soliton packets and their hyperchaotic properties at the MC band gap only. The hyperchaotic nature of dissipative soliton packets is confirmed by an estimation of the two highest Lyapunov exponents from the experimental time series. The modified Vyshkind-Rabinovich model demonstrates the self-generation of a dark pulse train at a decaying wave (MSSW) and a bright pulse train at the parametrically excited waves (the exchange spin waves) due to two saturation mechanisms. One of them is connected with the parametric instability, whereas the other one is caused by the increment nonlinearity. The developed self-generator may be of great interest to reservoir-computing that is based on the concept of "computation at the edge of chaos."

DOI: 10.1103/PhysRevApplied.21.044008

I. INTRODUCTION

Magnonic crystals (MCs) are one of the varieties of the magnetic metamaterials [1] containing an artificially created periodic structure, the period T of which is comparable to the spin-wave (SW) length λ [2–7]. The SW with a wave number satisfying the Bragg resonance condition ($k_B = n\pi/T$, where k_B is the Bragg wave number, $n = 1, 2, 3\cdots$ is the index of the Bragg resonance) is reflected from the periodic structure and does not pass to the MC output. It leads to the formation of band gaps in the SW spectrum that are analogues of the forbidden energy bands of a solid crystal lattice. The loss at the MC band-gap frequencies depend on the periodic structure length and tend to infinitely large values for the periodic structure of infinite length.

Nowadays, the one-dimensional (1D) [4,5,8], two-dimensional (2D) [3,5,8,9], and even three-dimensional (3D) [10] MCs have been created. Such MCs contain either one (single-component) [4,5,8] or two (bicomponent) [11,12] magnetic materials as well as the various types of the static defects [13–17]. The properties of the MCs were studied experimentally by the use of both microwave [4,14,17] and Brillouin light-scattering [5,8,17] techniques. The spin-wave mode localization appearing in such static MCs was caused by the presence of the demagnetizing fields arising at the edges of the periodic structure elements [8].

In magnonics, the dynamic MCs (DMCs) providing the band-gap control by a direct electric current are of great interest for the information storage systems and magnon logic [18,19]. In the first DMC construction, the direct electric current created the dynamic periodic structure due to the spatial periodic modulation of an internal magnetic field of an yttrium-iron-garnet (YIG) film. It led to the formation of the band gaps, the parameters of which (depth and width) were dynamically controlled by the changing value and polarity of the electric current [18]. In another DMC construction, the periodic structure was formed by etching the width of the YIG waveguide according to the periodic law and was static [19]. A magnonic band gap was located inside the magnetostatic surface spin-wave (MSSW) spectrum and was dynamically controlled by the direct electric current flowing through two conducting wires. Both wires were placed on a homogeneous part of the YIG waveguide near to its periodically modulated

*Corresponding author. sergrsh@yandex.ru

edges and were oriented perpendicularly to an external static magnetic field. In this case, the conducting wires created an additional static magnetic field that had opposite direction to the external static magnetic field. As a result, the internal magnetic field of the DMC had two minimums in the places of the conducting wire locations and their depths depended on the current values. Thus, the increase in the direct current values led to the fact that the periodic structure did not affect the MSSW propagation. However, in both DMC designs, the band gaps were dynamically controlled only in the linear regime.

In nonlinear magnonics, the MCs supporting four-wave nonlinear spin-wave interactions are used both to form the envelope gap solitons [20–23] and to create the various types of nonlinear functional devices: the signal-to-noise enhancers, the nonlinear phase shifters, and the switches [24,25]. The linear and nonlinear properties of the MCs are also used in the active ring resonators either to select a dominant ring eigenmode [26], or to reduce the phase noise of an oscillator [27], or to generate the chaotic dissipative envelope solitons [28]. In the last case, the chaotic pulse trains are formed inside the MC first band gap, when three- and four-wave nonlinear spin-wave interactions coexist.

In recent years, an active ring resonator based on a YIG waveguide supporting the MSSW propagation have been considered as the object for practical reservoir-computing (RC) applications [29]. Such a RC system exploited the delayed response and strong nonlinearity of the MSSW damping at high microwave power levels, for which the active ring resonator operated in the single-mode generation regime. However, there is a concept of "computation at the edge of chaos" that a RC system possesses maximal computational power at a phase transition between regular and chaotic regimes [30,31]. There is an analogy with the brain, which maximizes own information capacity operating near such a critical state [32]. In Ref. [33], the authors proposed the RC system based on the quenched chaos, that was observed in the coupled chaotic Lorenz oscillators. The "explosive death" of chaotic oscillations ensured the transition to the regular oscillations. In this case, the reservoirs still remained in a regular regime during computation, but were close enough to chaos. The information capacity values obtained for the RC system using the coupled chaotic oscillators were significantly higher than the ones obtained for the RC system based on the coupled regular phase oscillators.

In the paper, we represent a potential candidate for the RC applications that are based on the concept of "computation at the edge of chaos." It is the microwave active ring resonator with a delayed feedback loop that contains two nonlinear elements: a 1D MC supporting both three-wave nonlinear spin-wave processes of decay and confluence as well as a transistor amplifier operating in the output-power saturation mode. The 1D MC contains a dynamic line-defect—a conducting wire that is placed on the 1D MC surface. Such auto-oscillation system self-generates the sequences of hyperchaotic packets of dissipative dark envelope solitons, inside of which the envelope has chaotic behavior and outside them the envelope is approximately constant. The direct electric current flowing through the conducting wire greatly influences the durations of envelope time intervals of constant and chaotic amplitudes only when the self-generated signal is inside the MC band gap.

II. EXPERIMENT

A. Generator setup

In Fig. 1, there is a scheme of the active ring resonator that contains the 1D MC with the dynamic line defect, an amplifying stage consisting of three amplifiers and a variable attenuator. The 1D MC is the periodic structure of crests and grooves with $T = 200$ μm, that is formed on an YIG film surface with the use of etching and lithography techniques. The crests and grooves have the same width of 100 μm. The grooves are characterized by an etch depth of 1 μm. The 1D MC possessing a length of 4 mm is made from a 10-μm-thick YIG film with a width of 4 mm and a saturation magnetization of 1750 G. The dynamic line defect is created by the direct electric current flowing through a copper wire with a diameter of 100 μm and a length of 4.5 mm that is placed along the longitudinal symmetry axes of the MC. The distance between the conducting wire and the YIG surface is of about 100 μm, which makes it possible to exclude the effect of heating through the MSSW propagation. The excitation and detection of the MSSW propagating in the MC is realized by the use of two (input and output) microstrip transducers. Each transducer is 30 μm wide and 6 mm long. The distance between them is 6 mm. The external static magnetic field H_0 is in the plane and it is perpendicularly to both the direction of MSSW propagation and the copper wire. The choice of the bias magnetic field strength is due to creating conditions for three-wave nonlinear spin-wave interactions.

The amplifying stage consists of an input amplifier that is a five-resonant drift-klystron amplifier as well as the intermediate and output amplifiers that are the transistor amplifiers. A signal power level at the MC entrance is regulated by the variable attenuator and is measured by a two-channel power meter. It also controls a signal power level at the entrance of the output transistor amplifier operating in output-power saturation mode. A self-generated microwave signal is fed through the directional couplers to the entrances of a spectrum analyzer and a real-time oscilloscope for analysis and further processing. The oscilloscope is characterized by a 10 GHz passband, a signal sampling rate, and a memory depth equal to 20 GS/s and 2 million dots, respectively.

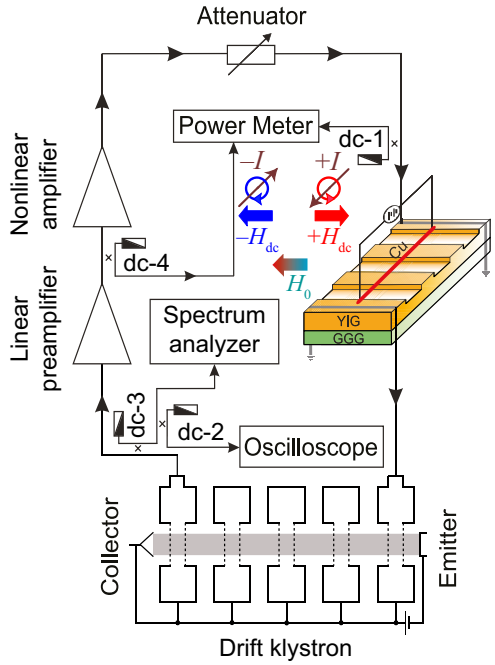

FIG. 1. The scheme of the active ring resonator containing the amplifying stage and the 1D magnonic crystal with dynamic line defect.

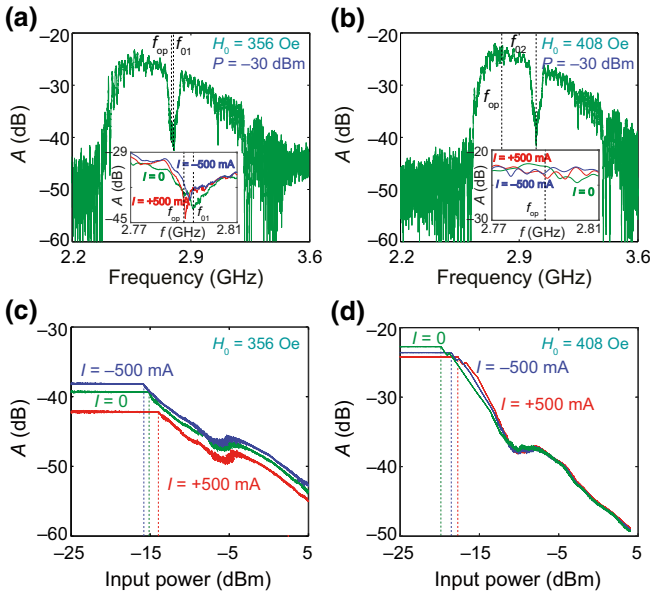

FIG. 2. The AFRs (a),(b) and the amplitude responses (c),(d) of the 1D MC measured in the absence (green solid lines) and the presence (red and blue solid lines) of the direct electric current. In (a),(c), the responses are obtained for $H_{01} = 356$ Oe and in (b),(d) they are obtained for $H_{02} = 408$ Oe. In (c), the measurements are carried out for $f_{op} \cong f_{01}$ and in (d) for $f_{op} \ll f_{02}$. The inserts in (a),(b) demonstrate the parts of the AFRs measured in the absence and the presence of the direct electric current of different polarities.

B. Magnonic crystal with dynamic line defect

In Figs. 2(a) and 2(b), the amplitude-frequency responses (AFRs) of the 1D MC measured by a network analyzer in linear operation mode are presented. The results are obtained for two values of H_0. For each H_0 value, three cases of the direct current applying to the copper wire are considered: (1) the direct current is not applied to the copper wire ($I = 0$); (2) the direct current of positive polarity (the current direction coincides with the direction of the MSSW propagation) is applied to the copper wire ($I > 0$); and (3) the direct current of negative polarity (the current direction is opposite to the direction of the MSSW propagation) is applied to the copper wire ($I < 0$). As follows from the results presented in Figs. 2(a) and 2(b), the MSSW spectra measured in the absence of direct current contain only one clear stopband corresponding to the MC first band gap with $k_{B1} = 157$ cm^{-1} at $n = 1$. For $H_{01} = 356$ Oe [see Fig. 2(a)], the stopband central frequency is $f_{01} = 2797$ MHz and for $H_{02} = 408$ Oe [see Fig. 2(b)] it is $f_{02} = 3000$ MHz.

There is an insert in Fig. 2(a) that shows a part of the AFR measured near the first band-gap frequency f_{01}, when the direct current of different polarities is applied to the wire. It can be seen that for the positive polarity current, the first band gap is shifted towards the low frequencies and for the negative polarity current it is shifted towards the high frequencies. In both cases, the direct current induces the magnetic induction (or the additional static magnetic field H_{dc}), the direction of which either is opposite to the H_0 direction (see corresponding illustration in Fig. 1 for the positive polarity current) or coincides with the H_0 direction (see corresponding illustration in Fig. 1 for the negative polarity current). The dependence of H_{dc} orientation on the direct current polarity is the main cause of the internal static magnetic field (H_{int}) manipulation in the line-defect region. For the positive polarity current, the H_{int} value in the line-defect region must be decreased and for the negative polarity current it must be increased. Further, we will confirm our assumptions with the results of numerical simulations.

An insert in Fig. 2(b) shows a part of the AFR measured far from the first band-gap frequency f_{02} at two direct current polarities. Although the influence of the induced magnetic field H_{dc} on the internal magnetic field H_{int} has the same character as in the previous case, however in contrast to the latter, the attenuation curve changes are less pronounced. In this case, the resonant properties of the band gap do not affect the signal attenuation levels.

Figures 2(c) and 2(d) demonstrate the management of the 1D MC amplitude responses by applying the direct electric current to the conducting wire. The measurements are carried out at an operating frequency $f_{op} = 2790$ MHz that is placed either inside the first band gap (the frequency f_{op} is slightly below the frequency f_{01} for $H_0 = 356$ Oe), or

outside the first band gap (the frequency f_{op} is placed far from the frequency f_{02} for $H_0 = 408$ Oe). For two H_0 values, the amplitude responses contain both linear and nonlinear sections. The linear section corresponds to the linear MSSW loss level and the nonlinear section corresponds to the nonlinear MSSW loss. The input-power threshold P_{th} possessing the microwatt values determines the beginning of the MC nonlinear operation mode due to the parametric three-wave decay of MSSW. This parametric three-wave process satisfies the following conditions:

$$\begin{aligned} \omega_p &= \omega_1 + \omega_2 + \delta, \\ k_p &= k_1 + k_2, \end{aligned} \tag{1}$$

where ω_p, k_p are the frequency and wave number of a pump wave (in our case, it is the decayed MSSW), $\omega_{1,2}$, $k_{1,2}$ are the frequencies and wave numbers of the parametrically excited waves and δ is a detuning of the parametrically excited wave frequencies from the half-value frequency of the decayed wave (the frequency detuning from synchronism). For the degenerate case, when $\omega_1 = \omega_2 = \omega_s$ and $\delta = 0$, the frequency ω_s is equal to $\omega_p/2$.

In Fig. 3, the dispersion characteristics of the dipole MSSW and the parametrically excited dipole-exchanged SWs (DESWs) are presented. The MSSW dispersion curve was calculated by the use of the Damon-Eschbach theory [34], and the DESW curves were calculated by the use of a dispersion equation obtained by Kalinkos and Slavin in the unpinnned surface spin approximation [35]. It can be seen, that the operating frequency f_{op} corresponding to the pump frequency is located in the MSSW spectrum and the half-value of the operating frequency ($f_{op}/2$) is placed in both the dipole backward volume MSW (BVMSW) and exchanged SW (ESW) spectra. If the operating frequency is fixed, then the increase in the H_0 value leads to the decrease in the MSSW wavenumber value k_{op} corresponding to the frequency f_{op}. In the last case, the frequency $f_{op}/2$ tends to the "bottom" of the DESW spectrum. It should be noted that the parametrically excited dipole BVMSW and ESWs propagating in the YIG film plane transversally to the MSSW direction of propagation can take part simultaneously in three-wave parametric confluence processes that can lead to the appearance of satellites of the first and second types [36,37].

Three-wave parametric decay of MSSW is a nonlinear process that begins from the threshold power level possessing a minimal value relative to the higher-order (for instance, four-wave) parametric spin-wave interactions. This threshold depends on the frequency, external static magnetic field, MSW wavenumber and saturation magnetization. For the fixed operating frequency located in the MSSW spectrum, the power threshold is decreased with increasing of H_0 value. It is due to the power threshold has a minimal value for the MSSW wave numbers placed near the ferromagnetic resonance frequency. The similar

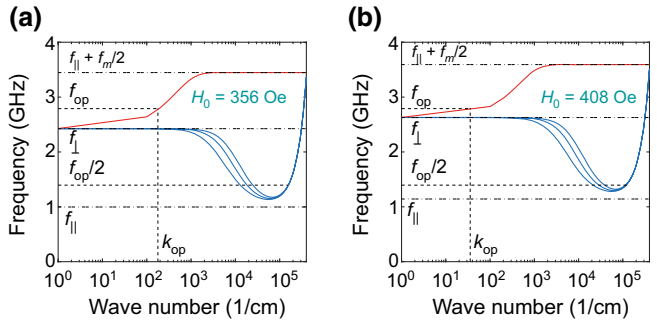

FIG. 3. The dispersion characteristics of the dipole MSSW and three first modes of the dipole-exchanged SWs obtained for two values of H_0: (a) 356 Oe and (b) 408 Oe. The calculation results are plotted on a semilogarithmic scale and performed for $f_{||} = \gamma H_0$, $f_\perp = \sqrt{f_{||}(f_{||} + f_m)}$, $f_m = 4\pi\gamma M_0$, $\gamma = 2.8$ MHz/Oe, $4\pi M_0 = 1750$ G, as well as for the YIG thickness 10 μm and for the exchange constant $q = 3 \times 10^{-12}$ cm^2.

trend is observed for the three-wave power thresholds presented in Figs. 2(c) and 2(d) in the absence of the direct current. So at $H_0 = 356$ Oe, the power threshold P_{th} has a value of -15 dBm that is decreased to a value of -20 dBm at $H_0 = 408$ Oe. Note, that the reflective properties of the MC first band gap do not affect the threshold of three-wave parametric processes, since the latter begin at the YIG film entrance before the start of the MSSW reflection from the periodic structure. The changes in the direct-current value from $+500$ to -500 mA give the same changes of the input-power thresholds of about 2 dB for two H_0 values. As a result, the dynamic range of the input-power threshold does not depend on the band-gap resonant properties.

In turn, the band-gap resonant properties great influence both linear and nonlinear MSSW loss. From the results presented in Fig. 2(c) it follows that the MSSW linear loss level is increased significantly for the direct current of positive polarity and decreased for the direct current of negative polarity. As a result, the dynamic range of the MSSW linear loss is of about 4 dB. It can be explained that for the positive polarity current, the band-gap frequency tends to the operating frequency and for the negative polarity current the band-gap frequency tends to move away from the operating frequency. As follows from the results presented in Fig. 2(d), the band-gap resonance properties do not greatly affect the MSSW linear loss level. In this case, the dynamic range of the MSSW linear loss is decreased to the value of 1.5 dB.

The highest dynamic range for the MSSW nonlinear loss is also observed for $H_0 = 356$ Oe. It has a maximum value of about 3 dB, when the input power exceeds the P_{th} (for $I = 0$) by 1 dB, and this value is practically constant for all higher P_{in} values. For $H_0 = 408$ Oe, the dynamic range of the MSSW nonlinear loss depends on the current polarity, only when the input power exceeds the P_{th} (for $I = 0$) no more than 7 dB only. For $P_{in} > -12$ dBm, the MSSW

nonlinear losses do not depend on the current polarity and remain constant. Thus, by applying the direct electric current of different polarity to the wire conductor, it becomes possible to control not only the MSSW linear loss, but also the MSSW nonlinear loss levels.

To confirm our assumptions about influence of the direct electric current polarity on the internal magnetic field transformation in the dynamic line-defect region, we calculated the spatial distributions of the H_{int} intensity for two values of both the current polarity and external static magnetic field. The calculations were performed using the COMSOL Multiphysics. The results of these calculations are presented in Figs. 4(a) and 4(b). It is shown that in the absence of the direct current, the H_{int} intensity is practically equal to the H_0 intensity ($H_{\text{int}} \cong H_0$) for the central part of the YIG waveguide that is typical for the tangentially magnetized YIG waveguides. The presence of the direct current of positive polarity leads to the decrease in the H_{int} intensity in the dynamic line-defect region, where $H_{\text{int}} \cong H_0 - H_{dc}$, and, vice versa, for the negative polarity current, the H_{int} intensity is increased in this region, where now $H_{\text{int}} \cong H_0 + H_{dc}$. For both values of H_0, the transformation of H_{int} value in the line-defect region is of about 10 Oe for $I = \pm 800$ mA and of about 2.5 Oe for $I = \pm 200$ mA.

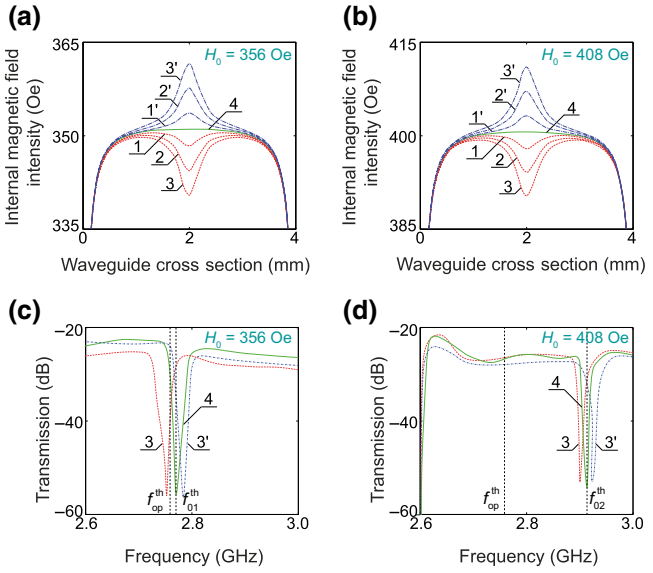

FIG. 4. (a),(b) The spatial distributions of the internal magnetic field intensity in the cross section of the 1D MC and (c),(d) the AFRs of the 1D MC calculated for the absence (solid green curves 4) and the presence (dashed curves) of the direct electric current of different polarities. Dashed red curves 1, 2, and 3 correspond to the positive polarity current of +200, +500, and +800 mA, respectively. Dashed blue curves 1', 2', and 3' correspond to the negative polarity current of −200, −500, and −800 mA, respectively. In (a),(b), the results are obtained for $d/2$ and in (c),(d), the ones are obtained for $I = \pm 800$ mA. In (a),(c), $H_0 = 356$ Oe and in (b),(d), $H_0 = 408$ Oe.

In the next step, we use the H_{int} profiles obtained in the COMSOL Multiphysics for various current polarities to simulate the 1D MC AFRs in the MuMax. In Fig. 4(c), there are simulation results that show how the H_{int} transformation affects the MC first band-gap shift for $H_0 = 356$ Oe. It is shown that for the positive polarity current, the band gap is shifted towards the low frequencies and, vice versa, for the negative polarity current the band gap is shifted towards the high frequencies. If the fitted operating frequency $f_{\text{op}}^{\text{th}}$ is slightly lower than the calculated first band-gap frequency f_{01}^{th} [see black dashed lines in Fig. 4(c)], then the MSSW linear losses are increased for the positive polarity current, and, vice versa, for the negative polarity current they are decreased. These results confirm the dependencies of the MSSW linear loss on the current polarity obtained in the experiment [see Fig. 2(c)].

In Fig. 4(d), we demonstrate the management of the MSSW linear loss in the absence of the calculated first band-gap frequency f_{02}^{th} near the operating frequency $f_{\text{op}}^{\text{th}}$. The AFR simulation was performed for $H_0 = 408$ Oe. It can be seen that, in contrast to the previous case, applying the direct current of different polarity does not lead to a significant change in the MSSW linear loss level near the frequency $f_{\text{op}}^{\text{th}}$. These results are in a good agreement with the experimental data presented in Fig. 2(d). Thus, the obtained simulation results clearly illustrate the transformation both the internal magnetic field and MSSW linear loss under the action of the direct electric current of different polarities.

C. Drift-Klystron and transistor amplifiers

The amplifying stage consists of the two broadband transistor amplifiers operating in the frequency range 2–4 GHz and the narrowband drift-klystron amplifier operating at the frequency of about 2.8 GHz. The drift-klystron amplifier and the intermediate (transistor) amplifier operate in the linear amplification mode and the output (transistor) amplifier operates in the output power saturation mode. In Fig. 5(a), the AFR of the drift-klystron amplifier measured in the linear operation mode is presented. It is shown, that the maximum signal amplification is observed at a central frequency of the klystron amplifier $f_0 = 2797$ MHz. When the drift-klystron amplifier is used in the ring generator scheme, the first band gap of the 1D MC is tuned to the frequency f_0. This is necessary in order to create the amplitude and phase conditions for the pulse signal generation in the band gap, where a duty factor of the pulse signal will be most effectively controlled by the direct electric current. The amplitude response of the transistor amplifier, that is the output amplifier of the amplifying stage, is shown in Fig. 5(b). The amplitude response measured at the frequency f_0 contains the nonlinear section, where the output power is saturated and remains practically constant in all input power region. In

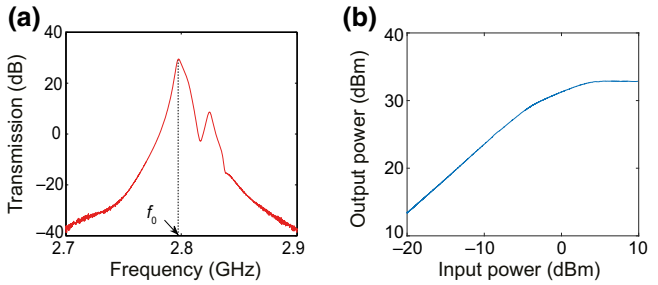

FIG. 5. (a) The AFR of the drift-klystron amplifier measured at the input power $P_{\text{in}} = -30$ dBm and (b) the amplitude response of the output transistor amplifier measured at the frequency $f_0 =$ 2797 MHz.

this nonlinear mode, the output amplifier operates in the ring generator.

D. Self-generation of hyperchaotic dissipative dark envelope solitons inside the band gap

1. Current control is absent

In Fig. 6, the power spectrum, time series, and phase portrait of the chaotic packets of dissipative dark envelop solitons are presented. The pulse trains are obtained at the ring gain $G = K - A = 31$ dB (where K is an amplifying stage gain and A is the total loss in the ring), when the direct electric current is not applied to the copper conductor ($I = 0$). In this case, the average power of the pulse signal measured at the MC entrance is $P_{\text{in}} = +3$ dBm exceeds the threshold of three-wave parametric decay by 18 dB. This is a value of a supercriticality parameter. The average power of the pulse signal measured at the output amplifier entrance (the second nonlinear element) is $P_{\text{in}} = +5$ dBm that corresponds to the saturation mode of the output power [see Fig. 5(b)].

From the results presented in Fig. 6(a), it follows that a microwave signal with a noiselike spectrum is self-generated at a ring resonator dominant eigenmode only, because the klystron amplifier limits the wide spectrum of the ring eigenmodes and does not allow the development of the multimode self-generation. The central frequency of the noiselike spectrum is located near the frequency f_{01}. In the time domain [see Fig. 6(b)], a dark envelope pulse packet train is formed. The pulse packets are self-generated through a balance between amplification and MSSW nonlinear loss produced by the nonlinear three-wave parametric decay. The MSSW dispersion is not involved in this balance. Such localized in time domain structures that are formed in an open, nonlinear, and nonequilibrium system can be classified as the dissipative solitons [38].

The amplitude and phase profiles of the dark pulse packets are calculated on the basis of the experimental time series, which are the first subject to digital processing for filtering of quantization noise, and then to the Hilbert

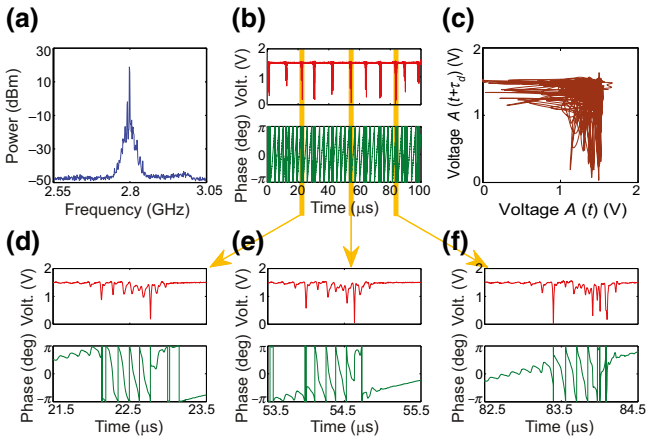

FIG. 6. The characteristics of the hyperchaotic train of pulse packets consisting of the dissipative dark envelope solitons measured for $H_0 = 356$ Oe: (a) the microwave power spectrum, (b),(d),(e),(f) the time series of the amplitude (upper panel) and phase (lower panel) of the envelope, and (c) the projections of a phase portrait on the parameter plane $(A(t), A(t+\tau_d))$, where $\tau_d = 100$ ns—a time delay of the ring resonator.

transformation. As a result of the mathematical processing, the microwave filling has been excluded from the further consideration and the phase ψ of the envelope has been determined as $\psi = \psi_0 - \omega_c t$, where ψ_0 is the total phase of the Hilbert-conjugated signals and ω_c is the frequency corresponding to that of the "center of masses" of the microwave signal spectrum. Note that the instantaneous phase determination via the Hilbert-conjugated signal is correct even in the case of the chaotic signal generation, since the signal spectrum contains a well-pronounced frequency for which the notion of instantaneous phase can be used [39].

As follows from the results presented in Figs. 6(b), 6(d)–6(f), the time intervals of approximately constant envelope are interrupted unpredictably by the time intervals of envelope chaotic oscillations. However, the time intervals of chaotic oscillations are much shorter than the time intervals of constant amplitude. Such unpredictable disruptions in the microwave signal generation can be classified as the "explosive death" of oscillations possessing the approximately constant amplitude and appearance of chaotic oscillations. This critical regime is the inverse of the "amplitude death" of large-amplitude chaotic oscillations [40], but also can be used in the RC systems supporting the concept of "computation at the edge of chaos."

Each dark envelope pulse packet has the averaged width T_{d1} of about 0.9 μs and the averaged repetition rate f_{am1} of about 100 kHz, which corresponds to the automodulation frequency of the ESWs parametrically excited by the decaying MSSW. The averaged duty factor q of the

pulse packets is about of 11. Each packet consists of several narrow "dips," the intensity and repetition interval of which are varied chaotically. The amplitude and phase profiles of the dips look like the amplitude and phase profiles of the dark envelope solitons. Usually, one of the dips of each packet, has the amplitude that drops to zero, and the phase that undergoes a jump of 180° inside the dip. The dip is similar to the black envelope soliton possessing a duration T_{d2} of about 30 ns that is determined by the bandwidth of the drift-klystron amplifier. For the remaining dips of a packet, the amplitude does not drop strictly to zero, and the phase inside it does not undergo a 180° jump. These dips look like the gray envelope solitons. As shown in Figs. 6(d)–6(f), the dark (gray) envelope pulses inside each packet have the averaged repetition rate f_{am2} of about 8 MHz, that corresponds to the first-order satellites [36]. Such satellites are the secondary MSSWs produced as a result of three-wave confluence processes of parametrically excited ESWs [37]. The four-wave nonlinear interactions are probably not observed in this experiment, since in the investigated single-mode system there is no multimode frequency comb inherent for such interactions [41]. The complex dynamics of the ring generator is evidenced by the "blurred" structure of the attractor [see Fig. 6(c)]. The phase portrait is plotted using the experimental time series and the Takens theorem [42], which is employed for attractor reconstruction from the experimental time series.

To confirm the chaotic nature of the envelope pulse packet train, two large LEs were calculated from the experimental time series. The calculations were carried out according to the algorithm described in Ref. [43]. It was found that both LEs are positive and have the values of $\lambda_1 = 1.61\ \mu s^{-1}$ and $\lambda_2 = 0.09\ \mu s^{-1}$. Their positive values indicate that the self-generated pulse packets of the dissipative dark envelope solitons are hyperchaotic.

In contrast to the hyperchaotic dark multisoliton complexes described in Ref. [44], the hyperchaotic dark pulse packets presented here possess more duration and have not partial chaotic synchronization of both the ring eigenmodes and the spin-wave automodulation frequencies. As a result, the narrow dark pulses embedded in long dark pulses do not have a clear quasiperiod, and their amplitude varies chaotically. Besides, two highest LEs calculated for the hyperchaotic dark multisoliton complexes described in Ref. [44] have the same order of magnitude, but in our case they differ by an order of magnitude.

Next, we will show the management both of the average duty factor of hyperchaotic pulse packets and the partial chaotic synchronization of the narrow dark envelope pulses inside the packets thought the change in the MSSW nonlinear loss level by applying the direct current of different polarities to the line-defect region.

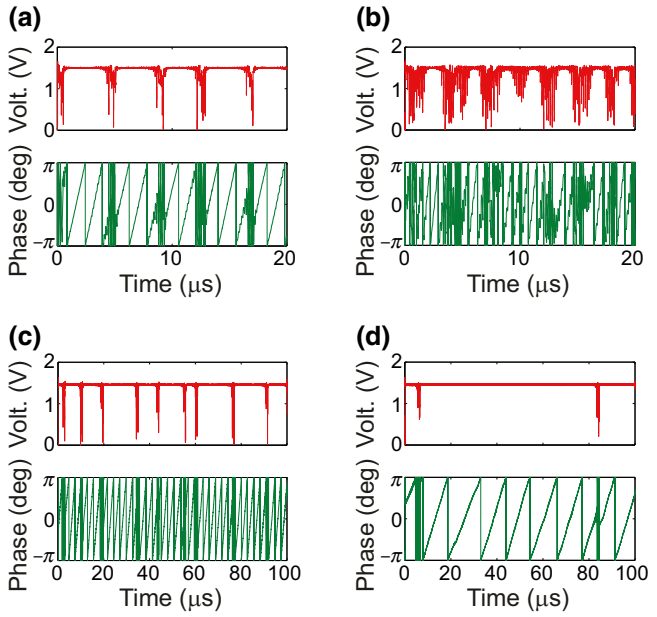

FIG. 7. The amplitude (upper panel) and phase (lower panel) profiles of the hyperchaotic train of pulse packets consisting of the dissipative dark envelope solitons measured for $H_0 = 356$ Oe for the direct electric current I of positive polarity: (a) +320 mA, (b) +800 mA and of negative polarity: (c) −100 mA and (d) −200 mA.

2. Current control is present

In Fig. 7, we demonstrate the dynamic control of the hyperchaotic packets of the dissipative dark envelope solitons by applying the direct electric current of different polarity to the wire conductor. At the positive polarity current $I = +320$ mA [see Fig. 7(a)], the averaged repetition rate of the pulse packets is increased to a value of about $f_{am1} \cong 250$ kHz (the averaged duty factor is decreased to $q \cong 4.4$), but the pulse packet width does not change. For this current polarity, the MSSW nonlinear loss level is increased [see Fig. 2(c)] and it leads to the increase in both the supercriticality parameter and associated with him the automodulation frequency of the parametrically excited SWs. The duration of the narrow dark envelope solitons embedded in the long dark pulses is not changed and their intensity and repetition interval vary still chaotically.

The characteristics of the envelope pulse packets begin to change strongly at $I = +800$ mA [see Fig. 7(b)]. In this case, the averaged repetition rate and the averaged width of the envelope pulse packets are increased to $f_{am1} \cong$ 350 kHz ($q \cong 1.6$). The number of narrow dark envelope pulses in each packet is increased and these envelope pulses have a clear quasiperiod. Some pulse packets have the form of a multisoliton complex, which contains repeating sequences of six narrow dark envelope solitons, the phase between them is varied by a value of about $\pi/3$.

Such pulse behavior can be explained by the creation of strong inhomogeneous decreasing internal magnetic field in the line-defect region at $I = +800$ mA [see Fig. 4(a)]. We believe that at the band-gap frequencies in the absence of the positive polarity current, the MSSW parametrically excites DESWs only near the microstrip line due to the MSSW reflection from the periodic structure, i.e., in the line-defect region at $I = 0$, there is no three-wave parametric decay of the MSSW. The applying of the positive polarity current leads to the decrease in the MSSW parametric threshold in the line-defect region (a MSSW wave number is increased here) and, as a consequence, to the parametric excitation of the ESWs in the line-defect region. The wave numbers of these ESWs are greater than the wave numbers of the ESWs parametrically excited by MSSW near the microstrip line, where the internal magnetic field intensity does not change. As a result, the frequency detuning $\triangle f$ from the frequency $f_{op}/2$ for such short-wave ESWs is decreased [45] in the line-defect region. In turn, the frequency detuning $\triangle f$ determines the value of the frequency f_{am2} appearing due to the three-wave parametric confluence processes. Thus, at $I = +800$ mA the interval of values of the automodulation frequency f_{am2} expands because the interval of ESW wave number expands too. It leads to the mutual overlap of the automodulation frequencies f_{am2} and their partial synchronization as well as to the increase in the pulse packet width.

For the positive polarity current, both LEs are positive and have the values of $\lambda_1 = 2.45\ \mu s^{-1}$, $\lambda_2 = 1.28\ \mu s^{-1}$ for $I = +320$ mA and $\lambda_1 = 8.88\ \mu s^{-1}$, $\lambda_2 = 5.17\ \mu s^{-1}$ for $I = +800$ mA. For this current polarity, both LEs grows and the difference between them is decreased. The LE values calculated for $I = +800$ mA practically correspond to the LE values obtained for hyperchaotic dark multisoliton complexes in Ref. [44].

For comparison, Fig. 8 shows the hyperchaotic dark multisoliton complexes obtained in two different experiments. One of them exploits the positive current-controlled 1D MC active ring resonator and the other uses the active ring resonator based on a L-shaped magnonic waveguide [44]. It is shown that in both experiments the amplitude of the narrow dark envelope pulses is increased from the edge of the long dark pulse to its central part. In contrast to the multisoliton complex shown in Fig. 8(a), the multisoliton complex presented in Fig. 8(b) contains repeated sequences of four narrow dark envelope pulses, the phase between which is varied by $\pi/2$.

For the negative polarity current [see Figs. 7(c) and 7(d)], the averaged repetition rate of the pulse packets is decreased and reaches the minimum value of about $f_{am1} = 13$ kHz (the averaged duty factor is increased to the maximum value $q \cong 80$) at $I = -200$ mA [see Fig. 7(d)]. The automodulation frequency f_{am2} appearing due to the three-wave parametric confluence processes and the pulse-packet width are practically constant in this case. It has the following explanation. In this case, the increasing internal magnetic field in the line-defect region [see Fig. 4(a)] provides the decrease in both the supercriticality parameter [see Fig. 2(c)] and associated with it the automodulation frequency f_{am1} appearing due to the three-wave parametric decay processes. The MSSW parametric threshold is increased in the line-defect region (a MSSW wave number is decreased) and ESWs are not excited here. Thus, the frequency detuning $\triangle f$ and associated with it the automodulation frequency f_{am2} does not change.

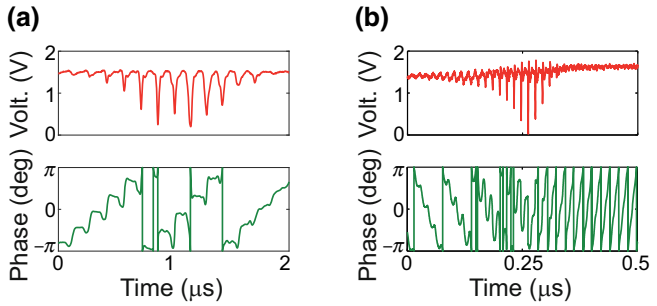

FIG. 8. The amplitude (upper panel) and phase (lower panel) profiles of the hyperchaotic dark multisoliton complexes obtained in the active ring resonators containing in a feedback loop either (a) the 1D MC possessing the dynamic line defect (for $I = +800$ mA and $H_0 = 356$ Oe) or (b) the L-shaped magnonic waveguide without dynamic control [44].

We also calculated the two highest LEs for the negative polarity current and found that for $I = -100$ mA they remain positive and equal to $\lambda_1 = 1.68\ \mu s^{-1}$, $\lambda_2 = 0.11\ \mu s^{-1}$. However, for $I = -200$ mA, only one large LE is positive $\lambda_1 = 0.3\ \mu s^{-1}$, while the other one becomes negative $\lambda_2 = -0.87\ \mu s^{-1}$. Thus, the variation of the current polarity from positive to negative leads not only to an increase in the duty factor of pulse packets by 50 times, but also to the change of the generation mode from hyperchaotic to chaotic.

E. Self-generation of hyperchaotic dissipative dark envelope solitons outside the band gap

1. Current control is absent

In Fig. 9, there are the results of the microwave pulse signal self-generation, when its carrier frequency is located outside the MC band gap. The dark pulse packets are obtained at the ring gain $G = 25.5$ dB, when the direct electric current is not applied to the copper conductor ($I = 0$). In this case, the average power of the pulse signal measured at the MC entrance is $P_{in} = +3$ dBm and at the output amplifier entrance is $P_{in} = +1.5$ dBm. For these power levels, both nonlinear elements operate in the nonlinear mode. As follows from the results presented in Fig. 9(a), the microwave signal with a noiselike spectrum is also self-generated at the frequency of the dominant ring eigenmode, which is located near the frequency f_{01}. In the

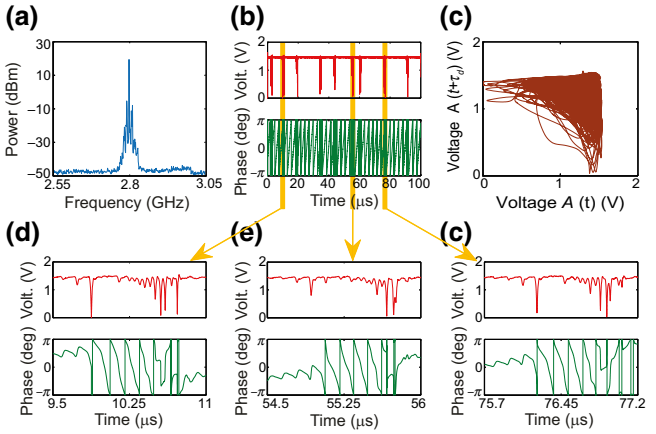

FIG. 9. The characteristics of the hyperchaotic train of pulse packets consisting of the dissipative dark envelope solitons measured for $H_0 = 408$ Oe: (a) the microwave power spectrum, (b),(d),(e),(f) the time series of the amplitude (upper panel) and phase (lower panel) of the envelope, and (c) the projections of a phase portrait on the parameter plane $(A(t), A(t+\tau_d))$.

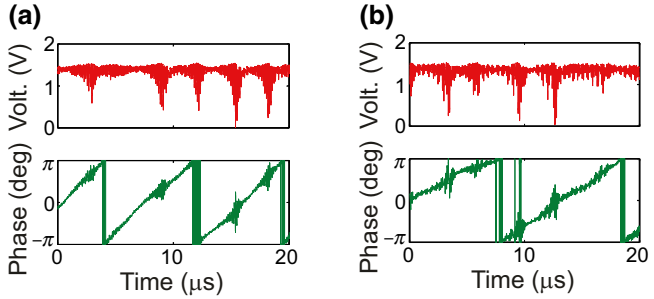

FIG. 10. The amplitude (upper panel) and phase (lower panel) profiles of the dissipative dark envelope soliton trains measured at $H_0 = 408$ Oe different type current polarity: (a) $I = +300$ mA and (b) $I = -300$ mA.

time domain [see Fig. 9(b)], the dark pulse packets containing the black and gray dissipative envelope solitons are formed. The averaged repetition rate of the pulse packets and their averaged duty factor q are the same values as for $H_0 = 356$ Oe. As shown in Figs. 9(d)–9(f), the dark (gray) envelope pulses located inside each packet have also the same repetition rate as in the previous case. For $H_0 = 408$ Oe, the complex dynamics of the ring generator is evidenced by the "blurred" structure of the attractor [see Fig. 9(c)]. It has a similar view as for $H_0 = 356$ Oe [see Fig. 6(c)]. Thus, the hyperchaotic packets of dissipative dark envelope solitons self-generated at $I = 0$ both inside and outside the MC band gap have similar characteristics at the same input-power level.

2. Current control is present

In Fig. 10, the dynamic control of the pulse packets through the applying the direct electric current of different polarity to the wire conductor is demonstrated. At the positive and negative polarity of the direct current, the averaged width T_{d1} and the averaged repetition rate f_{am1} are increased. In both cases, $f_{\text{am1}} \cong 300$ kHz and $q \cong 1.7$. Besides, for both current polarity, the dark pulse packets become wider than in the absence of current control. We have the following explanations for the observed phenomena. We assume that at the frequencies outside the band gap, in the absence of current, the DESWs can be parametrically excited by MSSW not only near the microstripe line, but also in the line-defect region, because there is no MSSW reflection from the periodic structure. Applying the direct current of different polarity leads to the excitation of DESWs, the wave numbers of which in the line-defect region differ from the wave numbers of DESWs excited near the microstrip line. It should be noted that the MSSW propagating in the line-defect region will have a power above the parametric threshold even for the negative polarity current. In this regard, the parametrically excited DESWs affect the width of dark pulse packets both for the positive and negative polarity current, that is observed in the experiment. Also we note, that the change in the current polarity leads to the increase in both the MSSW nonlinear loss level and the supercriticality parameter [see Fig. 2(d)]. As a result, the automodulation frequency f_{am1} is increased for both current polarities.

In contrast to the direct current control of the MSSW nonlinear loss level inside the band gap, two highest LEs remain positive both for positive and negative current polarity, when the direct current control of the MSSW nonlinear loss level is realized outside the band gap. So for the positive current polarity ($I = +300$ mA), $\lambda_1 = 2.21\ \mu\text{s}^{-1}$, $\lambda_2 = 0.68\ \mu\text{s}^{-1}$ and for the negative current polarity ($I = -300$ mA), $\lambda_1 = 4.22\ \mu\text{s}^{-1}$, $\lambda_2 = 2.21\ \mu\text{s}^{-1}$. Thus, if both the MSSW nonlinear loss level is increased only, then the transition from the hyperchaotic generation mode to the chaotic one is not observed.

III. MODIFIED VYSHKIND-RABINOVICH MODEL

The Vyshkind-Rabinovich model is a well-known parametric model created to describe turbulence in a dissipative medium with a hydrodynamic type of nonlinearity [46]. In this model, one of three parametrically interaction waves possessing linear increment is decayed into two waves that have damping in a linear approximation. The Vyshkind-Rabinovich model is described by three first-order ordinary differential equations that are written for the real variables. In Ref. [47], a similar model with one and a half freedom degrees was constructed for a ferromagnetic film active ring resonator supporting both the parametric decay of the MSSW into ESWs and the MSSW linear amplification. This model was developed on the basis of

the joint integration of the nonlinear motion equation of magnetization and the magnetostatic equations using the decomposition of the variable magnetization in terms of spin-wave modes and Green's tensor functions of the magnetostatic equations. Our modification of the Vyshkind-Rabinovich model is to use a nonlinear gain function. This approach allows us to describe the amplitude characteristic of a transistor amplifier, which does not have a falling section.

The suggested modified Vyshkind-Rabinovich model is developed to describe the formation of deep dips on the constant envelope background of the direct MSSW circulating in the active ring resonator. The model does not describe the interaction of direct and reflected MSSWs propagating in the 1D MC and it is valid only for the direct MSSW interacting with the parametrically excited SWs at some point in space. In such simple model, the MC bandgap influence on the direct MSSW nonlinear loss level and its dependence on the direct-current polarity will be taken into account through the fitting the frequency detuning from synchronism δ [see (1)]. As is well known, the parameter δ tends to the minimal values with decreasing of the supercriticality parameter and to the maximum values with increasing of it.

A model diagram of an active ring resonator containing two nonlinear elements is shown in Fig. 11. One of them is a ferromagnetic medium that supports the parametric decay of a high-frequency mode into two lower-frequency modes, for which condition (1) is satisfied. The other nonlinear element is an inertia-free amplifier, the output amplitude of which is saturated and remains constant with the increase in the input amplitude. It is assumed that the output and entrance of the previous nonlinear element are series connected with the entrance and output of the subsequent nonlinear element without delay. For such ring resonator, a modified Vyshkind-Rabinovich model is written as

$$\begin{aligned}
\frac{\partial m(t)}{\partial t} &= -c_0 b_1(t) b_2(t) \exp(-j\,\delta t) - \eta m(t) + \gamma \times \\
&\quad \times \{1 - \tanh[\alpha |m(t)|]\} m(t), \\
\frac{\partial b_1(t)}{\partial t} &= c_1 m(t) b_2^*(t) \exp(j\,\delta t) - \nu b_1(t), \\
\frac{\partial b_2(t)}{\partial t} &= c_2 m(t) b_1^*(t) \exp(j\,\delta t) - \nu b_2(t),
\end{aligned} \tag{2}$$

where $m(t)$ is the envelope complex amplitude of the decayed wave, $b_{1,2}(t)$ are the envelope complex amplitudes of two parametrically excited waves, γ is the linear increment of the decayed wave, α is its increment nonlinearity parameter, η is the decrement of the decayed wave, ν is the decrement of the parametrically excited waves, c_0, c_1, and c_2—the arbitrary coefficients.

If the increment nonlinearity parameter is equal to zero ($\alpha = 0$), then the modified Vyshkind-Rabinovich model (2) corresponds to the well-known Vyshkind-Rabinovich model [46,47]. The model (2) describes the dynamics of the dissipative systems possessing two saturation mechanisms. One of them due to the parametric decay and the other one is connected with the output amplitude saturation of the amplifier [see Fig. 5(b)].

The fitting of the frequency detuning from synchronism δ will be done for the one experimental case only, when the pulse sequences are self-generated inside the band gap. The fit will be considered as good, when the automodulation frequency f_{am1} of the calculated and experimental pulse sequences will coincide with each other.

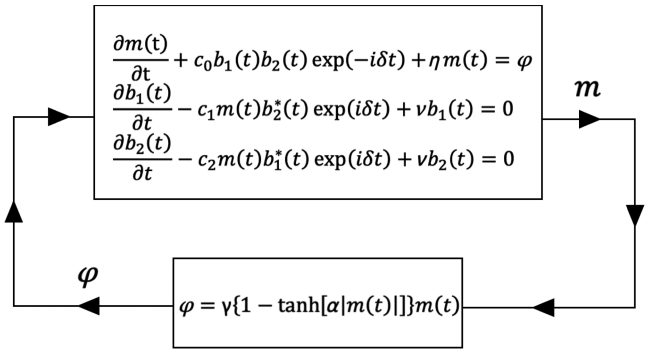

FIG. 11. The model diagram of the active ring resonator containing two nonlinear elements: a ferromagnetic medium supporting parametric three-wave decay (top element of the diagram) and a nonlinear amplifier (bottom element of the diagram).

IV. CALCULATION RESULTS

The system (2) of the first-order ordinary differential equations was solved by the fourth-order Runge-Kutta method. The values of the parameters c_0, c_1, and ν were taken from Ref. [47]. The increment nonlinearity parameter a was chosen in such a way that the amplitude of the decayed wave was limited by nonlinear amplification. We assume that the amplitudes of parametrically excited waves are equal to each other. In Fig. 12, there are the calculation results obtained for the modified Vyshkind-Rabinovich model, when the frequency detuning from synchronism δ is varied. It is shown that simultaneous presence of two saturation mechanisms is the reason for the formation of a flat amplitude plateau at the decayed wave. On this plateau, the periodic sequence of the narrow "dips" corresponding to the dark envelope pulses is observed. In contrast, the periodic sequence of the bright envelope pulses is formed on the parametrically excited waves. For the frequency detuning $\delta = 10^{-55}$ μs^{-1} [see Fig. 12(a)], the repetition rate of both dark and bright envelope pulses is of about 100 kHz that well corresponds to the experimental value of f_{am1} obtained for the long dark

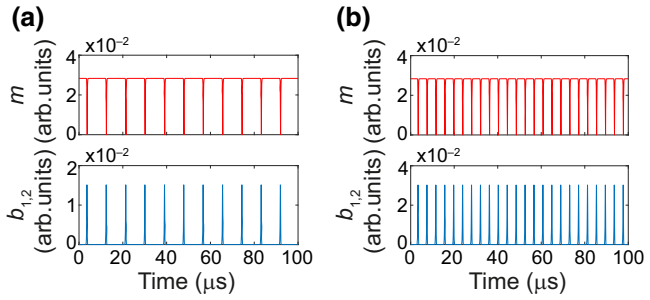

FIG. 12. The periodic sequences of the dark envelope pulses (upper panel) and bright envelope pulses (lower panel) calculated for two values of frequency detuning $\delta : 10^{-55}\ \mu s^{-1}$ (a) and $10^{-20}\ \mu s^{-1}$ (b). The calculations were performed for $c_0 = 1497\ \mu s^{-1}$, $c_1 = c_2 = 745\ \mu s^{-1}$, $\gamma = 45\ \mu s^{-1}$, $\nu = 9\ \mu s^{-1}$, $\eta = 5\ \mu s^{-1}$, and $\alpha = 50$.

pulse self-generation at $I = 0$ [see Fig. 6(b)]. Reducing the frequency detuning to $\delta = 10^{-20}\ \mu s^{-1}$ [see Fig. 12(b)] leads to increasing in the repetition rate of the dark and bright envelope pulses to the value of about 250 kHz. This value also well corresponds to the experimental value of f_{am1} obtained for the dark pulse self-generation in the band gap at $I = +320$ mA [see Fig. 7(a)]. As a result of numerical simulation of the experimental data obtained with the negative current polarity, we failed to obtain the repetition rate of about 10 kHz for the stationary pulse mode at the decreasing frequency detuning. This requires further improvement of the modified model to obtain a correspondence between the simulation results and the experimental data measured for $I = -200$ mA [see Fig. 7(d)].

V. CONCLUSIONS

In the paper, we experimentally investigated the critical regimes of the active ring resonator based on the 1D MC with the dynamic line defect. These regimes demonstrate the "explosive death" of the microwave oscillations of approximately constant amplitude and the birth of the chaotic amplitude oscillations in the dips of the envelope. The dip formation is a result of the joint action of two saturation mechanisms, one of which is caused by the output amplitude saturation of the nonlinear amplifier, and the other one by the amplitude saturation of the MSSW, leading to the parametric excitation of the dipole-exchange SWs. Both mechanisms of dip formation are confirmed by the calculation results obtained by the use of the modified Vyshkind-Rabinovich model. The nature of the chaotic oscillations inside the dips is connected with the nonlinear parametric three-wave confluence of the ESWs. The averaged period and the width of the dips depend on the MSSW nonlinear loss level that is controlled by the direct electric current flowing through the line-defect aria.

The direct electric current control of the MSSW loss level is based on the manipulation of the internal magnetic field intensity in the line-defect region. For the positive and negative polarity current, the internal magnetic field intensity is decreased and increased in this region, respectively, because the static magnetic field induced by the direct current has opposite direction to and coincides with the external static magnetic field direction. The current manipulation of the internal magnetic field leads to the band-gap shift towards the low and high frequencies for the positive and negative polarity current, respectively. If the self-generated signal frequency is inside the band gap, then the time intervals of approximately constant amplitude are either decreased or increased. In this case, two largest Lyapunov exponents are either both positive (the hyperchaotic mode) or one of them is positive and another is negative (the chaotic mode). The time intervals of approximately constant amplitude determine the duration of the information signal that can be introduced potentially to such magnonic reservoir for the reservoir computing.

The results obtained in this investigation are of great interest not only to specialists involved in the creation of the reservoir-computing systems supporting the concept of "computation at the edge of chaos" [30,31], but also to researchers in the field of nonlinear dynamics. For the last case, this is due to the experimental demonstration of the transition from hyperchaotic to chaotic dynamics in the auto-oscillation systems operating in the regime of "amplitude death."

ACKNOWLEDGMENTS

The study was supported by the Russian Science Foundation Grant No. 19-79-20121, [48].

[1] G. Dewar, Minimization of losses in a structure having a negative index of refraction, New J. Phys. **7**, 161 (2005).
[2] S. A. Nikitov, P. Tailhades, and C. S. Tsai, Spin waves in periodic magnetic structures - magnonic crystals, J. Magn. Magn. Mater. **236**, 320 (2001).
[3] V. V. Kruglyak, S. O. Demokritov, and D. Grundler, Magnonics, J. Phys. D: Appl. Phys. **43**, 264001 (2010).
[4] A. A. Serga, A. V. Chumak, and B. Hillebrands, YIG magnonics, J. Phys. D: Appl. Phys. **43**, 264002 (2010).
[5] G. Gubbiotti, S. Tacchi, M. Madami, G. Carlotti, A. O. Adeyeye, and M. P. Kostylev, Brillouin light scattering studies of planar metallic magnonic crystals, J. Phys. D: Appl. Phys. **43**, 264003 (2010).
[6] M. Krawczyk and D. Grundler, Review and prospects of magnonic crystals and devices with reprogrammable band structure, J. Phys.: Condens. Matter. **26**, 123202 (2014).
[7] A. V. Chumak, A. A. Serga, and B. Hillebrands, Magnonic crystals for data processing, J. Phys. D: Appl. Phys. **50**, 244001 (2017).

[8] R. Zivieri, Metamaterial properties of one-dimensional and two-dimensional magnonic crystals, Solid State Phys. **63**, 151 (2012).
[9] T. Schwarze, R. Huber, G. Duerr, and D. Grundler, Complete band gaps for magnetostatic forward volume waves in a two-dimensional magnonic crystal, Phys. Rev. B **85**, 134448 (2012).
[10] P. A. Popov, A. Y. Sharaevskaya, E. N. Beginin, A. V. Sadovnikov, A. I. Stognij, D. V. Kalyabin, and S. A. Nikitov, Spin wave propagation in three-dimensional magnonic crystals and coupled structures, J. Magn. Magn. Mater. **476**, 423 (2019).
[11] S. Tacchi, G. Duerr, J. W. Klos, M. Madami, S. Neusser, G. Gubbiotti, G. Carlotti, M. Krawczyk, and D. Grundler, Forbidden band gaps in the spin-wave spectrum of a two-dimensional bicomponent magnonic crystal, Phys. Rev. Lett. **109**, 137202 (2012).
[12] G. Gubbiotti, S. Tacchi, M. Madami, G. Carlotti, Z. Yang, J. Ding, A. O. Adeyeye, and M. Kostylev, Collective spin excitations in bicomponent magnonic crystals consisting of bilayer permalloy/Fe nanowires, Phys. Rev. B **93**, 184411 (2016).
[13] V. V. Kruglyak, M. L. Sokolovskii, V. S. Tkachenko, and A. N. Kuchko, Spin-wave spectrum of a magnonic crystal with an isolated defect, J. Appl. Phys. **99**, 08C906 (2006).
[14] Y. A. Filimonov, E. S. Pavlov, S. L. Vysotskii, and S. A. Nikitov, Magnetostatic surface wave propagation in a one-dimensional magnonic crystal with broken translational symmetry, Appl. Phys. Lett. **101**, 242408 (2012).
[15] H. Yang, G. Yun, and Y. Cao, Coupling characteristics of point defects modes in two-dimensional magnonic crystals, J. Appl. Phys. **112**, 103911 (2012).
[16] B. T. Schwarze and D. Grundler, Magnonic crystal wave guide with large spin-wave propagation velocity in CoFeB, Appl. Phys. Lett. **102**, 222412 (2013).
[17] M. A. Morozova, S. V. Grishin, A. V. Sadovnikov, D. V. Romanenko, Y. P. Sharaevskii, and S. A. Nikitov, Band gap control in a line-defect magnonic crystal waveguide, Appl. Phys. Lett. **107**, 242402 (2015).
[18] A. V. Chumak, T. Neumann, A. A. Serga, B. Hillebrands, and M. P. Kostylev, A current-controlled, dynamic magnonic crystal, J. Phys. D: Appl. Phys. **42**, 205005 (2009).
[19] A. A. Nikitin, A. B. Ustinov, A. A. Semenov, A. V. Chumak, A. A. Serga, V. I. Vasyuchka, E. Lähderanta, and B. A. Kalinikos, A spin-wave logic gate based on a width-modulated dynamic magnonic crystal, Appl. Phys. Lett. **106**, 102405 (2015).
[20] N. N. Chen, A. N. Slavin, and M. G. Cottam, Spin-wave envelope solitons in periodically modulated magnetic films, IEEE Trans. Magn. **28**, 3306 (1992).
[21] M. Dragoman and D. Jäger, Microwave gap solitons and bistability in magnetostatic periodic structures, Appl. Phys. Lett. **62**, 110 (1993).
[22] N. N. Chen, A. N. Slavin, and M. G. Cottam, Gap solitons in periodic structures: Modulated magnetic thin films, Phys. Rev. B **47**, 8667 (1993).
[23] A. B. Ustinov, B. A. Kalinikos, V. E. Demidov, and S. O. Demokritov, Formation of gap solitons in ferromagnetic films with a periodic metal grating, Phys. Rev. B **81**, 180406(R) (2010).
[24] A. B. Ustinov, A. V. Drozdovskii, and B. A. Kalinikos, Multifunctional nonlinear magnonic devices for microwave signal processing, Appl. Phys. Lett. **96**, 142513 (2010).
[25] M. A. Morozova, O. V. Matveev, D. V. Romanenko, A. V. Trukhanov, Y. P. Mednikov, A. M. Sharaevskii, and S. A. Nikitov, Nonlinear spin wave switches in layered structure based on magnonic crystals, J. Magn. Magn. Mater. **508**, 166836 (2020).
[26] A. D. Karenowska, A. V. Chumak, A. A. Serga, J. F. Gregg, and B. Hillebrants, Magnonic crystal based forced dominant wavenumber selection in a spin-wave active ring, Appl. Phys. Lett. **96**, 082505 (2010).
[27] E. Bankowski, T. Meitzler, R. S. Khymyn, V. S. Tiberkevich, A. N. Slavin, and H. X. Tang, Magnonic crystal as a delay line for low-noise auto-oscillators, Appl. Phys. Lett. **107**, 122409 (2015).
[28] S. V. Grishin, Y. P. Sharaevskii, S. A. Nikitov, E. N. Beginin, and S. E. Sheshukova, Self-generation of chaotic dissipative soliton trains in active ring resonator with 1-D magnonic crystal, IEEE Trans. Magn. **47**, 3716 (2011).
[29] S. Watt and M. Kostylev, Reservoir computing using a spin-wave delay-line active-ring resonator based on yttrium-iron-garnet film, Phys. Rev. Appl. **13**, 034057 (2020).
[30] C. G. Langton, Computation at the edge of chaos: Phase transitions and emergent computation, Phys. D **42**, 12 (1990).
[31] R. Legenstein and W. Maass, Edge of chaos and prediction of computational performance for neural circuit models, Neural Netw. **20**, 323 (2007).
[32] J. Beggs and D. Plenz, Neuronal avalanches in neocortical circuits, J. Neurosci. **23**, 11167 (2003).
[33] J. Choi and P. Kim, Reservoir computing based on quenched chaos, Chaos Solit. Fractals **140**, 110131 (2020).
[34] R. W. Damon and J. R. Eschbach, Magnetostatic modes of a ferromagnet slab, J. Phys. Chem. Solids **19**, 308 (1961).
[35] B. A. Kalinikos and A. N. Slavin, Theory of dipole-exchange spin wave spectrum for ferromagnetic films with mixed exchange boundary conditions, J. Phys. C: Solid State Phys. **19**, 7013 (1986).
[36] A. M. Mednikov, Nonlinear effects under the propagation of surface spin waves in YIG films, Sov. Phys. Solid State **23**, 136 (1981).
[37] A. G. Temiryazev, Conversion of the frequency of a surface magnetostatic wave under three-magnon decay conditions, Sov. Phys. Solid State **29**, 179 (1987).
[38] N. Akhmediev and A. Ankiewicz, *Dissipative Solitons: From Optics to Biology and Medicine* (Springer-Verlag, Berlin, 2008).
[39] V. S. Anishchenko, V. Astakhov, A. Neiman, and T. Vadivasova, *Nonlinear Dynamics of Chaotic and Stochastic Systems: Tutorial and Modern Developments (Springer Series in Synergetics)* (Springer, Springer Berlin, Heidelberg, 2007), 2nd ed.
[40] M.-D. Wei and J.-C. Lun, Amplitude death in coupled chaotic solid-state lasers with cavity-configuration-dependent instabilities, Appl. Phys. Lett. **91**, 061121 (2007).

[41] M. Wu, Nonlinear spin waves in magnetic film feedback rings, Solid State Phys. **62**, 163 (2010).
[42] F. Takens, Detecting strange attractors in turbulence, Lect. Notes Math. **898**, 336 (1981).
[43] A. Wolf, J. B. Swift, H. L. Swinney, and J. A. Vastano, Determining Lyapunov exponents from a time series, Phys. D **16**, 285 (1985).
[44] A. S. Bir, S. V. Grishin, O. I. Moskalenko, A. N. Pavlov, M. O. Zhuravlev, and D. O. Ruiz, Experimental observation of ultrashort hyperchaotic dark multisoliton complexes in a magnonic active ring resonator, Phys. Rev. Lett. **125**, 083903 (2020).
[45] G. A. Melkov and S. V. Sholom, Parametric excitation of spin waves by a surface magnetostatic wave, Sov. Phys. JETP **69**, 403 (1989).
[46] S. Y. Vyshkind and M. I. Rabinovich, The phase stochastization mechanism and the structure of wave turbulence in dissipative media, Sov. Phys. JETP **44**, 292 (1976).
[47] V. E. Demidov and N. G. Kovshikov, Mechanism for the appearance and randomization of the self-modulation of high-intensity spin waves, Tech. Phys. **44**, 960 (1999).
[48] https://rscf.ru/en/project/19-79-20121/

Correction: A second affiliation was inserted for the last author.